

# An alumina phase induced composite transition shuttle to stabilize carbon capture cycles

Received: 26 February 2024

Accepted: 21 August 2024

Published online: 30 August 2024

Check for updates

Xingyue Ma<sup>1,2</sup>, Shuxuan Luo<sup>1,2</sup>, Yunhui Hua<sup>3</sup>, Seshadri Seetharaman<sup>4</sup>, Xiaobo Zhu<sup>5</sup>, Jingwei Hou<sup>6</sup> , Lei Zhang<sup>6</sup> <sup>1,2</sup>, Wanlin Wang<sup>6</sup> <sup>1,2</sup> & Yongqi Sun<sup>6</sup> <sup>1,2</sup>

Limiting global warming to 1.5–2 °C requires a 50–90% reduction in CO<sub>2</sub> emissions in 2050, depending on different scenarios, and carbon capture, utilization, and storage is a promising technology that can help reach this objective. Calcium oxide (CaO) carbon capture is an appealing choice because of its affordability, large potential capacity, and ability to withstand the high temperatures of flue gases. However, the structural instability and capacity fading challenge its large-scale industrial applications. Here, we design a reversible reaction shuttle in CaO-based sorbents to improve the structure stability by changing the initial alumina phases. Diverse alumina phases (x-Al<sub>2</sub>O<sub>3</sub>) are first synthesized and utilized as the aluminum source for creating CaO@x-Al<sub>2</sub>O<sub>3</sub> composites. As expected, the CaO@δ-Al<sub>2</sub>O<sub>3</sub> composite demonstrates a carbon capture capacity of 0.43 g-CO<sub>2</sub>/g-sorbent after 50 cycles, with an impressive capacity retention of 82.7%. Combined characterizations and calculations reveal that this stability improvement is attributed to a transition shuttle between Ca<sub>3</sub>Al<sub>2</sub>O<sub>6</sub> and Ca<sub>5</sub>Al<sub>6</sub>O<sub>14</sub>, which can effectively restrain the complete decompositions of those structure-stabilized intermediate phases. An economic assessment further identifies the significance of heat transfer efficiency improvement upon cycles, and control of capital/operation cost, energy price and carbon tax for a future cost-effective commercialization of current strategy.

Implementing measures to reduce emissions, and exploring CO<sub>2</sub> capture, utilization and storage (CCUS) technologies are important steps to achieve the global 1.5 °C climate goal<sup>1–6</sup>, especially considering the incomplete substitution of fossil fuels globally in the coming decades<sup>7–9</sup>. In the context of CCUS, CO<sub>2</sub> capture stage accounts for ~70% of the total cost of the process, mostly due to the substantial decarbonation energy input<sup>4,6,10</sup>. Given this, it is crucial to develop an

affordable capture technique for its widespread use in industries. Compared to the low-temperature carbon capture sorbents such as amine-based sorbents, solid CaO emerges as a particularly advantageous material, characterized by its low cost and high theoretical CO<sub>2</sub> capture capacity (0.786 g-CO<sub>2</sub>/g-CaO)<sup>6,11,12</sup>. Notably, its intrinsic benefit lies in its aptitude for operation at high temperatures-carbonation within 500–850 °C and decarbonation at 850–1000 °C<sup>7,9,13</sup>. This aligns

<sup>1</sup>School of Metallurgy and Environment, Central South University, Changsha, China. <sup>2</sup>National Center for International Cooperation of Clean Metallurgy, Central South University, Changsha, China. <sup>3</sup>Residues and Resource Reclamation Centre, Nanyang Environment and Water Research Institute, Nanyang Technological University, Singapore, Singapore. <sup>4</sup>Department of Materials Science and Engineering, Royal Institute of Technology, Stockholm, Sweden. <sup>5</sup>College of Materials Science and Engineering, Changsha University of Science and Technology, Changsha, China. <sup>6</sup>School of Chemical Engineering, The University of Queensland, St Lucia, Australia. e-mail: [jingwei.hou@uq.edu.au](mailto:jingwei.hou@uq.edu.au); [wanlin.wang@csu.edu.cn](mailto:wanlin.wang@csu.edu.cn); [yongqi.sun@csu.edu.cn](mailto:yongqi.sun@csu.edu.cn)

well with the high-temperature nature of flue gases (>500 °C), allowing for the utilization of sensible heat in flue gases for sorbent decarbonation through strategically designed heat compensation approaches.

Pure CaO faces challenges to maintain its high CO<sub>2</sub> capture capacity during the repeated carbonation/decarbonation cycles. The working temperature of CaO-based sorbents is higher than the Tamman temperature of CaCO<sub>3</sub> (~530 °C), which accelerates the particle sintering and structure failure, as well as deactivation upon cycling<sup>14,15</sup>. Several strategies have been devised to improve its anti-sintering property and cyclic stability, such as preparation of nanosized CaO to augment reaction areas<sup>16</sup>, implementation of a hollow core-shell texture to accommodate volume expansion/contraction<sup>17</sup>, and the incorporation of inert supports such as Al<sub>2</sub>O<sub>3</sub>, MgO, SiO<sub>2</sub> and Y<sub>2</sub>O<sub>3</sub>, to bolster anti-sintering capability<sup>18–22</sup>.

Al<sub>2</sub>O<sub>3</sub> accounts for a representative inert support for structure stabilization, and the formation of ultrastable intermediate phases, such as Ca<sub>12</sub>Al<sub>14</sub>O<sub>33</sub>, Ca<sub>3</sub>Al<sub>2</sub>O<sub>6</sub> and CaAl<sub>2</sub>O<sub>4</sub>, is very important for sorbent stabilization<sup>22–33</sup>. Previous studies have largely concentrated on a single aluminum source especially  $\gamma$ -Al<sub>2</sub>O<sub>3</sub> as a structural matrix for CaO, neglecting the role of diverse Al<sub>2</sub>O<sub>3</sub> phases and their further distinct influences on the formation and transitions of intermediate phases<sup>22–33</sup>. In this case, the newly formed intermediate phases in the CaO@Al<sub>2</sub>O<sub>3</sub> composites after calcination are determined by an equilibrium reaction, which also results in a limited improvement of cyclic stability<sup>27,29,31–33</sup>. Al<sub>2</sub>O<sub>3</sub> exhibits multiple phases such as  $\gamma$ -,  $\theta$ -,  $\delta$ -, and  $\alpha$ -Al<sub>2</sub>O<sub>3</sub>, each possessing distinct characteristics, such as surface area, structural disorder, and thermodynamic stability<sup>34,35</sup>. Those unique properties could further affect their reaction with CaO as well as the formation of local intermediate phases, therefore influencing the effectiveness of structure stabilization upon cycling.

In this study, we tune the intermediate phases in the CaO@Al<sub>2</sub>O<sub>3</sub> composites by using various Al<sub>2</sub>O<sub>3</sub> phases ( $\gamma$ ,  $\delta$ ,  $\delta\&\theta$  and  $\alpha$ ). The CaO@ $\delta$ -Al<sub>2</sub>O<sub>3</sub> composite exhibits outstanding CO<sub>2</sub> capture performance, boasting an impressive ~82.7% capacity retention after 50 cycles, in stark contrast to the ~27.8% observed for pure CaO. Our exploration reveals the coexistence of two intermediate phases, specifically Ca<sub>3</sub>Al<sub>2</sub>O<sub>6</sub> and Ca<sub>5</sub>Al<sub>6</sub>O<sub>14</sub>, within the CaO@ $\delta$ -Al<sub>2</sub>O<sub>3</sub> composite. Further characterizations and calculations confirm a reversible transition between those phases, which curtails their decomposition during high-temperature cycling. An economic assessment substantiates the commercial viability of the present innovative strategy, which revolves around augmenting heat transfer efficiency and meticulously managing energy prices and carbon taxes.

## Results

### Varying alumina phases to target induce CaO@Al<sub>2</sub>O<sub>3</sub> composites

The fabrication process of CaO@ $x$ -Al<sub>2</sub>O<sub>3</sub> composites, directed by the equilibrium phase transitions within a binary CaO-Al<sub>2</sub>O<sub>3</sub> system (Fig. 1a), comprises two primary steps. Firstly, different alumina phases are synthesized through directly calcining  $\gamma$ -Al<sub>2</sub>O<sub>3</sub> phase at specific temperatures (Fig. 1b, c). Secondly, the resulting  $x$ -Al<sub>2</sub>O<sub>3</sub> (where  $x$  includes  $\gamma$ ,  $\delta$ ,  $\delta\&\theta$  and  $\alpha$ ) is mixed with calcium acetate and then further sintered under an air atmosphere (Fig. 1b, c). This leads to the formation of target CaO@ $x$ -Al<sub>2</sub>O<sub>3</sub> composites, characterized by diverse intermediate phases including Ca<sub>3</sub>Al<sub>2</sub>O<sub>6</sub> and Ca<sub>5</sub>Al<sub>6</sub>O<sub>14</sub> (Fig. 1d, e). According to the CaO-Al<sub>2</sub>O<sub>3</sub> phase transitions (Fig. 1a), Ca<sub>3</sub>Al<sub>2</sub>O<sub>6</sub> is the only intermediate phase with a CaO/Al<sub>2</sub>O<sub>3</sub> mass ratio of 8:2. Nevertheless, we fabricate more intermediate phases by using varying  $x$ -Al<sub>2</sub>O<sub>3</sub> phases at a same CaO/Al<sub>2</sub>O<sub>3</sub> mass ratio in this study.

Alumina X-ray diffraction (XRD) patterns (Fig. 1d) reveal a phase transition from  $\gamma$ -Al<sub>2</sub>O<sub>3</sub> to new  $\delta$ - and  $\theta\&\delta$ -Al<sub>2</sub>O<sub>3</sub> following calcination at 900 and 1000 °C, respectively. Both phases show weak-crystallinity XRD patterns due to their high structural disorder. In comparison,  $\alpha$ -

Al<sub>2</sub>O<sub>3</sub> calcined at 1200 °C shows a higher crystallinity as well as a stronger thermal stability<sup>35</sup>. XRD patterns of the CaO@ $x$ -Al<sub>2</sub>O<sub>3</sub> composites (Fig. 1e) exhibit the strong characteristic peaks of CaO. Ca<sub>3</sub>Al<sub>2</sub>O<sub>6</sub> is formed when  $\gamma$ -,  $\delta$ - and  $\theta\&\delta$ -Al<sub>2</sub>O<sub>3</sub> are used as aluminum source. Interestingly, as the alumina phase changes from  $\gamma$ - to  $\delta$ -,  $\theta\&\delta$ - and  $\alpha$ -Al<sub>2</sub>O<sub>3</sub>, a new Ca<sub>5</sub>Al<sub>6</sub>O<sub>14</sub> phase is generated in the composites. It should be pointed out that the CaO/Al<sub>2</sub>O<sub>3</sub> mass ratio in those intermediate phases (such as Ca<sub>3</sub>Al<sub>2</sub>O<sub>6</sub> and Ca<sub>5</sub>Al<sub>6</sub>O<sub>14</sub>) is much less than the initial ratio of 8:2, indicating dominant CaO is used for CO<sub>2</sub> capture. Residual  $\alpha$ -Al<sub>2</sub>O<sub>3</sub> is found in CaO@ $\alpha$ -Al<sub>2</sub>O<sub>3</sub> composite with very limited Ca<sub>5</sub>Al<sub>6</sub>O<sub>14</sub> phase (Supplementary Fig. 1). This highlights the importance of alumina phase regulation to tune the formation of intermediate phases in final CaO@ $x$ -Al<sub>2</sub>O<sub>3</sub> composites.

From the X-ray photoelectron spectroscopy (XPS, Supplementary Figs. 2–4), we identify lower binding energies of the Al 2p spectra in CaO@ $\gamma$ -Al<sub>2</sub>O<sub>3</sub>, CaO@ $\delta$ -Al<sub>2</sub>O<sub>3</sub>, CaO@ $\theta\&\delta$ -Al<sub>2</sub>O<sub>3</sub> composites than CaO@ $\alpha$ -Al<sub>2</sub>O<sub>3</sub> composite. Al only exhibits AlO<sub>4</sub> tetrahedral coordination in the intermediate phases of Ca<sub>5</sub>Al<sub>6</sub>O<sub>14</sub> and Ca<sub>3</sub>Al<sub>2</sub>O<sub>6</sub><sup>28</sup>. However, the  $\alpha$ -Al<sub>2</sub>O<sub>3</sub> and Ca<sub>5</sub>Al<sub>6</sub>O<sub>14</sub> phases in CaO@ $\alpha$ -Al<sub>2</sub>O<sub>3</sub> composite consist of both AlO<sub>6</sub> octahedral and AlO<sub>4</sub> tetrahedral coordination. A decrease in the coordination number of Al could result in a lower binding energy in the Al 2p XPS (Supplementary Fig. 2b)<sup>36</sup>, as will be further proved by solid state <sup>27</sup>Al MAS-NMR tests. In this case, the XPS results prove a more efficient use of alumina in CaO@ $\delta$ -Al<sub>2</sub>O<sub>3</sub> and CaO@ $\theta\&\delta$ -Al<sub>2</sub>O<sub>3</sub> composites, agreeing with the Raman spectra results (Supplementary Figs. 5, 6)<sup>37,38</sup>. A further variation of the CaO/Al<sub>2</sub>O<sub>3</sub> mass ratios (6:4 and 4:6) generates abundant intermediate phases for CaO@ $\gamma$ -Al<sub>2</sub>O<sub>3</sub> composites in a wide composition range (Supplementary Figs. 7,8). This specific Ca<sub>3</sub>Al<sub>2</sub>O<sub>6</sub> and Ca<sub>5</sub>Al<sub>6</sub>O<sub>14</sub> intermediate phase pair can be induced as varying CaO/ $\delta$ -Al<sub>2</sub>O<sub>3</sub> mass ratios (6:4, 7.6:2.4, 8:2 and 9:1) (Supplementary Fig. 9).

### Morphology and microstructures of CaO@Al<sub>2</sub>O<sub>3</sub> composites

All composites feature abundant porous structures (Supplementary Fig. 10) created by the decomposition of calcium acetate with the release of CO<sub>2</sub> and gaseous H<sub>2</sub>O. Those porous structures provide pathways for the diffusion of CO<sub>2</sub> and increase the reaction between CO<sub>2</sub> and CaO. The fabricated composites have similar specific surface areas (Supplementary Fig. 11) and even distributions of Ca and O elements, with a relatively uneven distribution of Al element due to its multiple phases. Based on the high resolution transmission electron microscope (HRTEM), we identify the intermediate phases in CaO@ $x$ -Al<sub>2</sub>O<sub>3</sub> composites (Fig. 2a–d). In the CaO@ $x$ -Al<sub>2</sub>O<sub>3</sub> composites, a 0.269 nm interplanar spacing is attributed to Ca<sub>3</sub>Al<sub>2</sub>O<sub>6</sub>, while a 0.289 nm interplanar spacing is assigned to Ca<sub>5</sub>Al<sub>6</sub>O<sub>14</sub>. Alongside those intermediate phases, an interplanar spacing of 0.237 nm corresponds to  $\alpha$ -Al<sub>2</sub>O<sub>3</sub>. Interplanar spacings of 0.277 nm and 0.240 nm are assigned to CaO. The obtained HRTEM results align with the XRD patterns.

To clarify the formation of intermediate phases in CaO@ $x$ -Al<sub>2</sub>O<sub>3</sub> composites induced by different alumina phases, we calculate the Gibbs free energy change ( $\Delta G$ ) of a reaction between CaO and various alumina phases to form Ca<sub>3</sub>Al<sub>2</sub>O<sub>6</sub> at 900 °C (Supplementary Table 1). As the alumina varies from  $\alpha$ -,  $\delta$ -, to  $\gamma$ -Al<sub>2</sub>O<sub>3</sub>,  $\Delta G$  becomes more negative. This could cause a larger amount of Ca<sub>3</sub>Al<sub>2</sub>O<sub>6</sub> when using  $\gamma$ -Al<sub>2</sub>O<sub>3</sub> as an aluminum source over other alumina phases. We further measure the solid-state <sup>27</sup>Al magic-angle spinning-nuclear magnetic resonance (<sup>27</sup>Al MAS-NMR) spectra of  $x$ -Al<sub>2</sub>O<sub>3</sub> (Fig. 2e). Two peaks centered at approximately 8 and 74 ppm confirm the presence of tetrahedral (AlO<sub>4</sub>) and octahedral (AlO<sub>6</sub>) coordinated Al-O units and their fractions are quantified (Supplementary Table 2). As the alumina varies from  $\gamma$ -,  $\delta$ -,  $\delta\&\theta$ -, to  $\alpha$ -Al<sub>2</sub>O<sub>3</sub>, the AlO<sub>6</sub> concentration gradually increases (from 65.9 to 92.2%) with less AlO<sub>4</sub>. In  $\alpha$ -Al<sub>2</sub>O<sub>3</sub>, AlO<sub>6</sub> is the dominant structural unit with limited AlO<sub>4</sub>. Those stable AlO<sub>6</sub> should first convert into AlO<sub>4</sub> and then react with CaO to form calcium

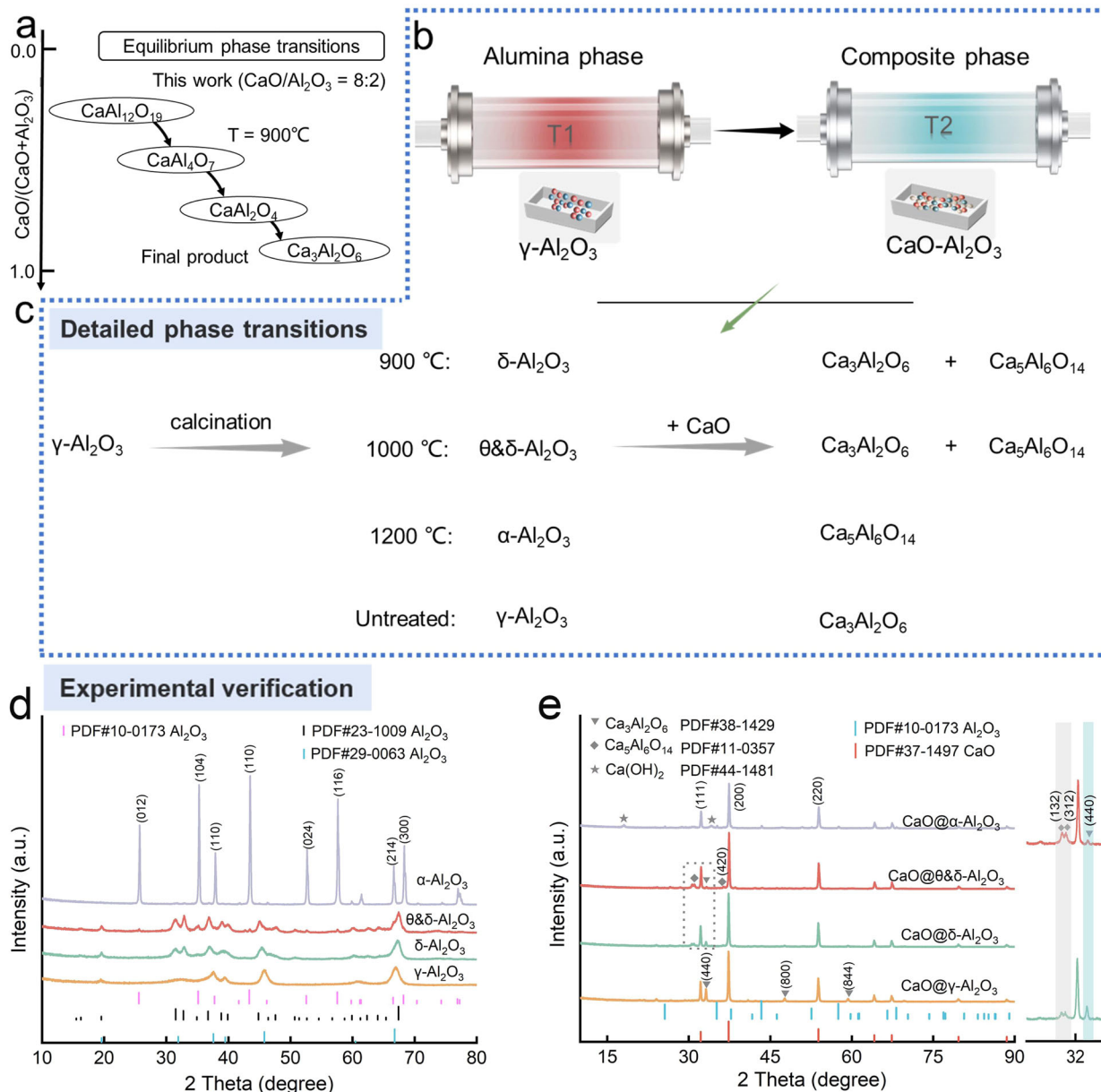


**Fig. 1 | Alumina phases induce CaO@Al<sub>2</sub>O<sub>3</sub> composites.** **a** Equilibrium phase transitions in a binary CaO-Al<sub>2</sub>O<sub>3</sub> system, which show the intermediate phases formed at varying CaO/Al<sub>2</sub>O<sub>3</sub> mass ratios at 900 °C. **b** Fabrication process of CaO@x-Al<sub>2</sub>O<sub>3</sub> composites include alumina phase regulation and composite

synthesis. **c** Detailed phase changes during the fabrication process. **d** XRD patterns of the newly synthesized x-Al<sub>2</sub>O<sub>3</sub> phases by calcining  $\gamma$ -Al<sub>2</sub>O<sub>3</sub> at different temperatures. **e** XRD patterns of the CaO@x-Al<sub>2</sub>O<sub>3</sub> composites.

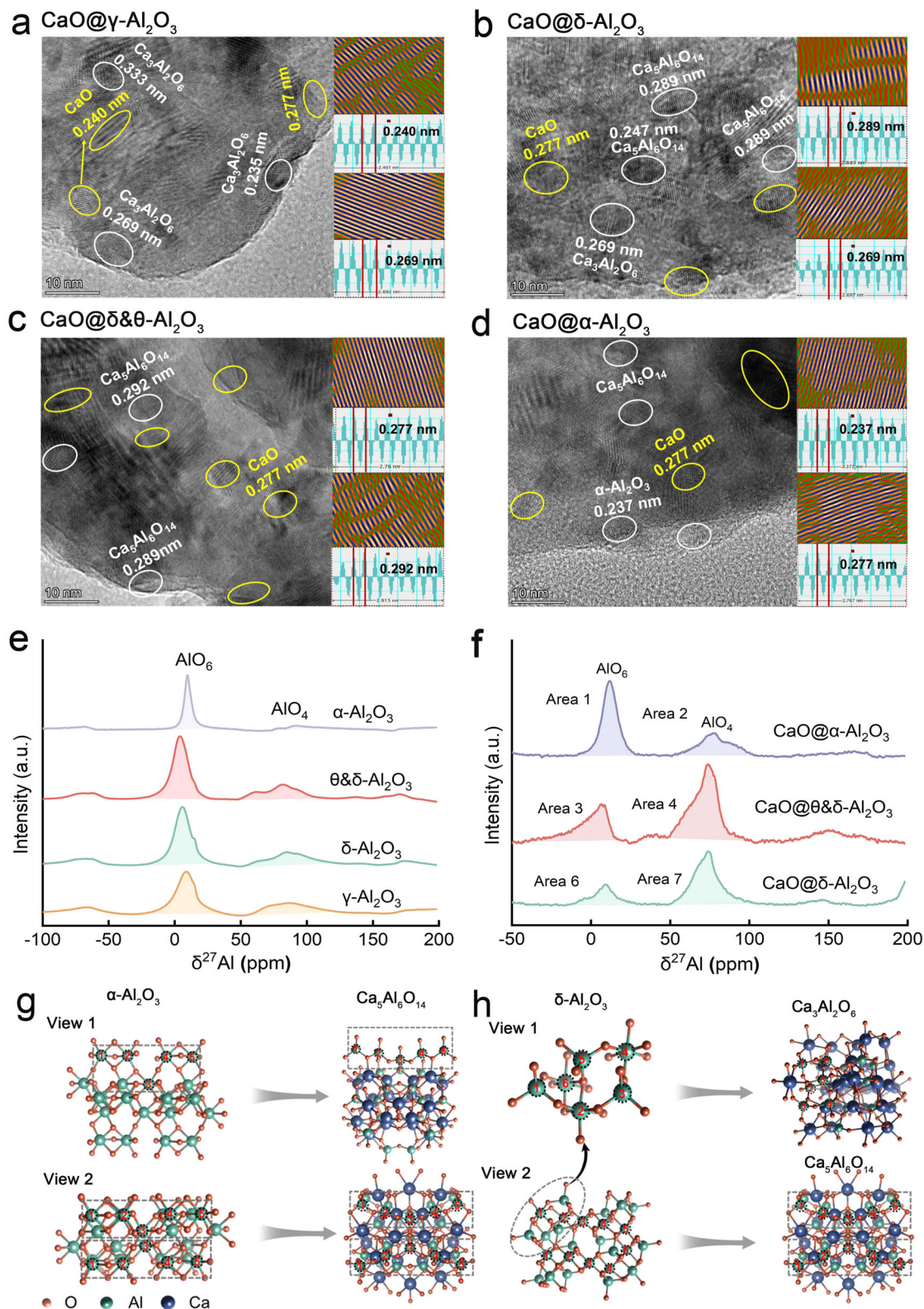
aluminates (Fig. 2g). In comparison,  $\delta$ -Al<sub>2</sub>O<sub>3</sub> with more AlO<sub>4</sub> units can directly react with CaO and thus remain in the formed calcium aluminates (Fig. 2h). The structure similarity between alumina and calcium aluminates causes the distinct reaction activities between alumina and CaO, and thus the formation of different intermediate phases.

To further explore the intermediate phases in the fresh CaO@ $\delta$ -Al<sub>2</sub>O<sub>3</sub>, CaO@ $\theta$ & $\delta$ -Al<sub>2</sub>O<sub>3</sub>, and CaO@ $\alpha$ -Al<sub>2</sub>O<sub>3</sub> composites, we measure their solid-state <sup>27</sup>Al MAS-NMR (Fig. 2f) and further quantify their relative amounts. As aforementioned, in both Ca<sub>5</sub>Al<sub>6</sub>O<sub>14</sub> and Ca<sub>3</sub>Al<sub>2</sub>O<sub>6</sub>, Al sites are predominantly in AlO<sub>4</sub>, while AlO<sub>6</sub> is attributed to alumina only. Therefore, there are residual alumina in CaO@ $\delta$ -Al<sub>2</sub>O<sub>3</sub>, CaO@ $\theta$ & $\delta$ -Al<sub>2</sub>O<sub>3</sub> and CaO@ $\alpha$ -Al<sub>2</sub>O<sub>3</sub> composites. We find that CaO@ $\delta$ -Al<sub>2</sub>O<sub>3</sub> composite exhibits a lower ratio of AlO<sub>6</sub> to AlO<sub>4</sub> (0.33) compared to CaO@ $\theta$ & $\delta$ -Al<sub>2</sub>O<sub>3</sub> (0.52) and CaO@ $\alpha$ -Al<sub>2</sub>O<sub>3</sub> (1.85) composites (Supplementary Table 3). This indicates that CaO@ $\delta$ -Al<sub>2</sub>O<sub>3</sub> composite has

the highest amount of intermediate phases or the highest use of alumina, which agrees with the XPS results (Supplementary Fig. 2b).

### CO<sub>2</sub> capture performances

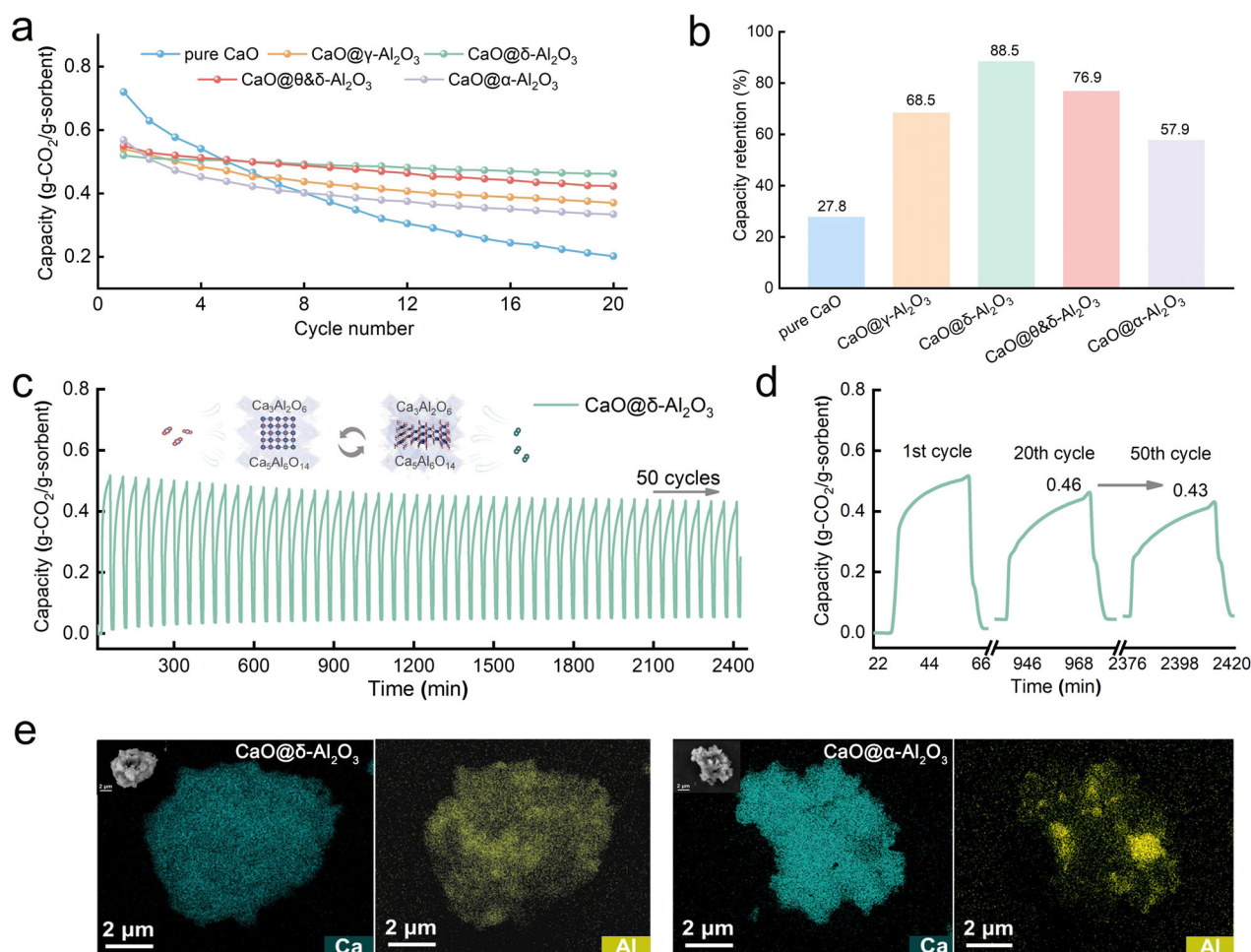
Those CaO@x-Al<sub>2</sub>O<sub>3</sub> composites have similar initial CO<sub>2</sub> capture capacities as the amount of reactive CaO are similar (Fig. 3a and Supplementary Figs. 12, 13). After 20 cycles, CaO@ $\delta$ -Al<sub>2</sub>O<sub>3</sub> composite exhibits the highest capacity retention of 88.5% (0.46 g-CO<sub>2</sub>/g-sorbent), surpassing CaO@ $\theta$ & $\delta$ -Al<sub>2</sub>O<sub>3</sub> of 76.9% (0.42), CaO@ $\gamma$ -Al<sub>2</sub>O<sub>3</sub> of 68.5% (0.37), and CaO@ $\alpha$ -Al<sub>2</sub>O<sub>3</sub> of 57.9% (0.33) (Fig. 3b). Notably, CaO@ $\delta$ -Al<sub>2</sub>O<sub>3</sub> and CaO@ $\theta$ & $\delta$ -Al<sub>2</sub>O<sub>3</sub> composites show enhanced CO<sub>2</sub> capture stability over the CaO@ $\gamma$ -Al<sub>2</sub>O<sub>3</sub> composite, which could be attributed to the coexistence of Ca<sub>3</sub>Al<sub>2</sub>O<sub>6</sub> and Ca<sub>5</sub>Al<sub>6</sub>O<sub>14</sub> phases in the composites and the stabilization effect. In comparison, the pure CaO without alumina shows the highest initial CO<sub>2</sub> capture capacity (0.73 g-CO<sub>2</sub>/g-sorbent) but with a very low retention rate of 27.8%



**Fig. 2 | Intermediate phase identification of  $\text{CaO}@x\text{-Al}_2\text{O}_3$  composites.**

**a–d** HTEM images with interplanar spacing characterization of  $\text{CaO}@x\text{-Al}_2\text{O}_3$  composites: **(a)**  $\text{CaO}@ \gamma\text{-Al}_2\text{O}_3$ , **(b)**  $\text{CaO}@ \delta\text{-Al}_2\text{O}_3$ , **(c)**  $\text{CaO}@ \theta\&\delta\text{-Al}_2\text{O}_3$ , and **(d)**  $\text{CaO}@ \alpha\text{-Al}_2\text{O}_3$ . **e**, **f** Solid-state  $^{27}\text{Al}$  MAS-NMR spectra: **(e)**  $\gamma\text{-Al}_2\text{O}_3$ ,  $\delta\text{-Al}_2\text{O}_3$ ,  $\theta\&\delta\text{-Al}_2\text{O}_3$  and  $\alpha\text{-Al}_2\text{O}_3$ .

and  $\alpha\text{-Al}_2\text{O}_3$ , **(f)** fresh  $\text{CaO}@ \delta\text{-Al}_2\text{O}_3$ ,  $\text{CaO}@ \theta\&\delta\text{-Al}_2\text{O}_3$  and  $\text{CaO}@ \alpha\text{-Al}_2\text{O}_3$  composites. **g**, **h** Structural comparisons: **(g)**  $\alpha\text{-Al}_2\text{O}_3$  with  $\text{Ca}_5\text{Al}_6\text{O}_{14}$ , **(h)**  $\delta\text{-Al}_2\text{O}_3$  with  $\text{Ca}_3\text{Al}_2\text{O}_6$  and  $\text{Ca}_5\text{Al}_6\text{O}_{14}$  at different views.



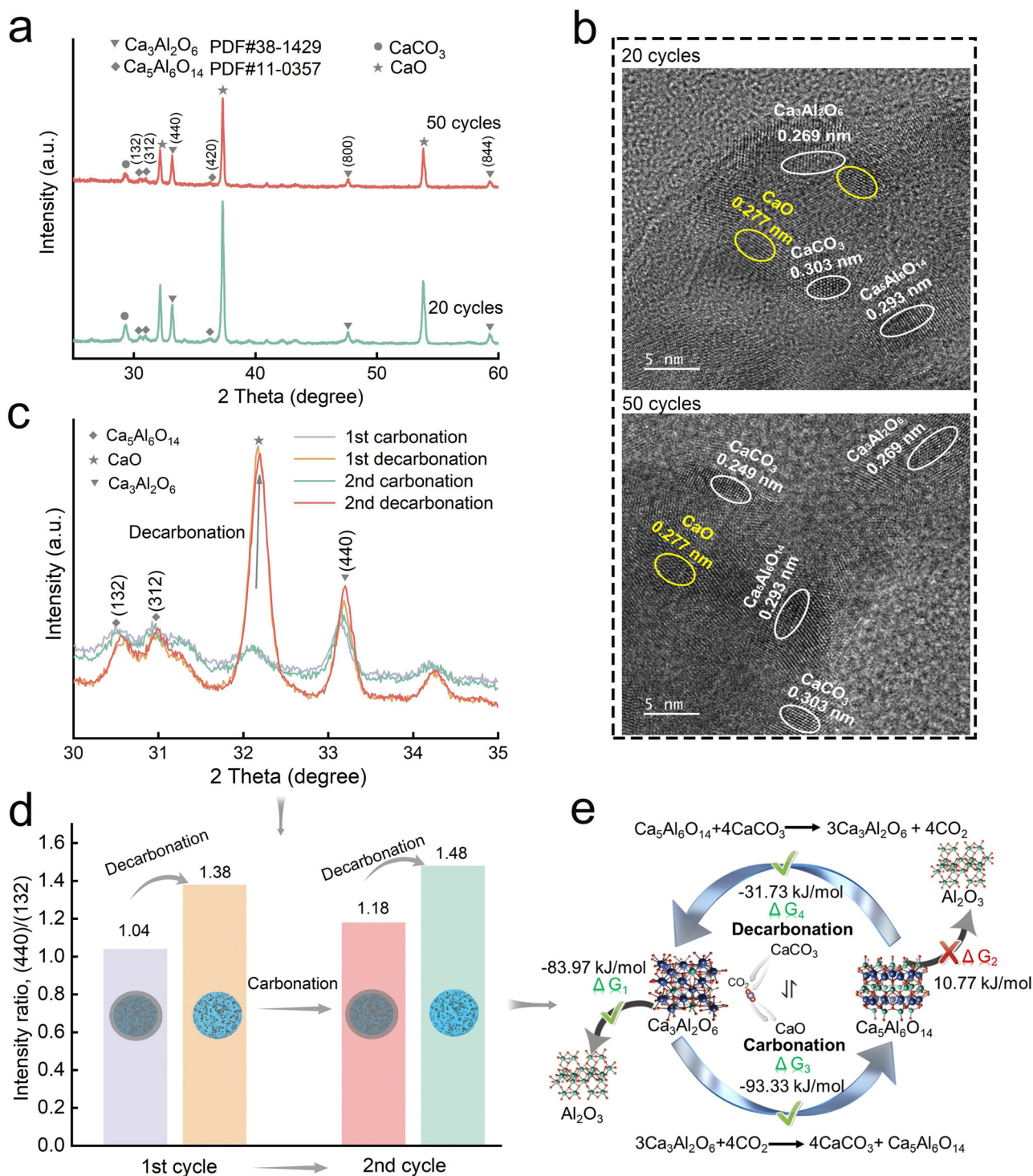


**Fig. 4 | A composite transition shuttle between  $\text{Ca}_3\text{Al}_2\text{O}_6$  and  $\text{Ca}_5\text{Al}_6\text{O}_{14}$  to stabilize  $\text{CO}_2$  capture cycles. a–c** Phase and structure analyzes upon the carbonation/decarbonation cycles: (a) XRD patterns and (b) HTEM images after 20 or 50 cycles of the  $\text{CaO}@ \delta\text{-Al}_2\text{O}_3$  composite; (c) XRD patterns of the  $\text{CaO}@ \delta\text{-Al}_2\text{O}_3$  composite after the 1st and 2nd carbonation/decarbonation cycles. **d** A schematic diagram of the conversion relationship between  $\text{Ca}_3\text{Al}_2\text{O}_6$  and  $\text{Ca}_5\text{Al}_6\text{O}_{14}$  during the

$\text{CO}_2$  capture process, mainly reflected in the peak intensity ratio of  $\text{Ca}_3\text{Al}_2\text{O}_6$ -(440) to  $\text{Ca}_5\text{Al}_6\text{O}_{14}$ -(132) from (c). **e** A summary diagram of the composite transition shuttle between  $\text{Ca}_3\text{Al}_2\text{O}_6$  and  $\text{Ca}_5\text{Al}_6\text{O}_{14}$  where  $\Delta G$  values are used to show the conversion directions (✓ indicates that the reaction can proceed and × indicates not).

performance. We further find  $\text{CaO}@ \delta\text{-Al}_2\text{O}_3$  and  $\text{CaO}@ \theta\&\delta\text{-Al}_2\text{O}_3$  composites show better  $\text{CO}_2$  capture performance than other samples, with the the coexistence of  $\text{Ca}_5\text{Al}_6\text{O}_{14}$  and  $\text{Ca}_3\text{Al}_2\text{O}_6$  in those two composites. Regarding  $\text{CaO}@ \gamma\text{-Al}_2\text{O}_3$  composite, it is noteworthy that  $\text{Ca}_3\text{Al}_2\text{O}_6$  alone also enhances  $\text{CO}_2$  capture stability compared to pure

$\text{CaO}$ , albeit to a lesser extent than observed with  $\text{CaO}@ \delta\text{-Al}_2\text{O}_3$ . Instead of a  $\text{Ca}_5\text{Al}_6\text{O}_{14}$  and  $\text{Ca}_3\text{Al}_2\text{O}_6$  pair in the  $\text{CaO}@ \delta\text{-Al}_2\text{O}_3$ ,  $\text{Ca}_3\text{Al}_2\text{O}_6$  could also remain in the  $\text{CaO}@ \gamma\text{-Al}_2\text{O}_3$  composite to stabilize the first 20 cycles'  $\text{CO}_2$  capture (Supplementary Fig. 21), which agrees with the reported results<sup>24,27,28,30,31</sup>.

To experimentally investigate the working mechanism of  $\text{Ca}_3\text{Al}_2\text{O}_6$  and  $\text{Ca}_5\text{Al}_6\text{O}_{14}$ , slow scanning XRD patterns of the  $\text{CaO}@ \delta\text{-Al}_2\text{O}_3$  composite are collected after the 1st and 2nd cycles to quantify the amount ratios of those two intermediate phases (Fig. 4c, d and Supplementary Table 6). During the 1st decarbonation stage (900 °C), the relative amount of  $\text{Ca}_3\text{Al}_2\text{O}_6$  to  $\text{Ca}_5\text{Al}_6\text{O}_{14}$  increases, as indicated by an increased main peak intensity ratio of  $\text{Ca}_3\text{Al}_2\text{O}_6$  (440) to  $\text{Ca}_5\text{Al}_6\text{O}_{14}$  (132). During the 2nd carbonation stage, the relative amount of  $\text{Ca}_3\text{Al}_2\text{O}_6$  to  $\text{Ca}_5\text{Al}_6\text{O}_{14}$  decreases, and it increases again during the 2nd decarbonation stage (Supplementary Table 6). Those results show a consistent conversion relationship between two intermediate phases. This involves a transition from  $\text{Ca}_3\text{Al}_2\text{O}_6$  to  $\text{Ca}_5\text{Al}_6\text{O}_{14}$  during the carbonation stage, stabilizing  $\text{Ca}_3\text{Al}_2\text{O}_6$  from being completely decomposed into alumina as well as the  $\text{CO}_2$  capture conversion between  $\text{CaO}$  and  $\text{CaCO}_3$ . Subsequently,  $\text{Ca}_5\text{Al}_6\text{O}_{14}$  converts back to  $\text{Ca}_3\text{Al}_2\text{O}_6$  during the decarbonation stage. The transition reactions between  $\text{Ca}_5\text{Al}_6\text{O}_{14}$  and  $\text{Ca}_3\text{Al}_2\text{O}_6$  are further verified by the in-situ XRD results (Supplementary Fig. 22) during the 1st and 2nd  $\text{CO}_2$  capture cycles. This newly found transition enriches the material design for  $\text{CaO}$ -based  $\text{CO}_2$  capture using the classical binary  $\text{CaO}$ - $\text{Al}_2\text{O}_3$  system, and the longevity of this transition is demonstrated even after 20 cycles (Supplementary Fig. 23). Additionally, this transition still works as varying  $\text{CaO}/\delta\text{-Al}_2\text{O}_3$  mass ratios (7.6:2.4 and 9:1), detailed in Supplementary Fig. 24.

To verify this result in theory, the  $\Delta G$  of those conversion reactions of  $\text{Ca}_3\text{Al}_2\text{O}_6$  and  $\text{Ca}_5\text{Al}_6\text{O}_{14}$  into alumina at various reaction temperatures are calculated (Fig. 4e and Supplementary Table 7). During the carbonation stage at 700 °C, the  $\Delta G$  of  $\text{Ca}_3\text{Al}_2\text{O}_6$  decomposition into alumina is  $-83.97$  kJ/mol, indicating a spontaneous reaction. Under the same condition, the  $\Delta G$  of  $\text{Ca}_5\text{Al}_6\text{O}_{14}$  decomposition into alumina is  $10.77$  kJ/mol, indicating a non-spontaneous reaction. However, for the phase transition from  $\text{Ca}_3\text{Al}_2\text{O}_6$  to alumina, the formation of  $\text{Ca}_5\text{Al}_6\text{O}_{14}$  could be an important intermediate state. In order to verify this, the  $\Delta G$  of  $\text{Ca}_3\text{Al}_2\text{O}_6$  decomposition into  $\text{Ca}_5\text{Al}_6\text{O}_{14}$  is calculated to be a more negative value of  $-93.33$  kJ/mol. This proves that  $\text{Ca}_3\text{Al}_2\text{O}_6$  would not totally decompose into alumina but an intermediate  $\text{Ca}_5\text{Al}_6\text{O}_{14}$  would be preferred in  $\text{CO}_2$  atmosphere. Another key aspect is that the transformation of  $\text{Ca}_3\text{Al}_2\text{O}_6$  into  $\text{Ca}_5\text{Al}_6\text{O}_{14}$  relies on the originally existed  $\text{Ca}_5\text{Al}_6\text{O}_{14}$ , which could indicate that the initial  $\text{Ca}_5\text{Al}_6\text{O}_{14}$ , formed by regulating the alumina phase to  $\delta\text{-Al}_2\text{O}_3$ , works as nucleation sites for the further formation of  $\text{Ca}_5\text{Al}_6\text{O}_{14}$  from  $\text{Ca}_3\text{Al}_2\text{O}_6$ . During the decarbonation stage at 900 °C,  $\text{Ca}_5\text{Al}_6\text{O}_{14}$  will react with  $\text{CaCO}_3$  and convert back to  $\text{Ca}_3\text{Al}_2\text{O}_6$ , as proved by a negative  $\Delta G$  of this reaction ( $-31.73$  kJ/mol). This reversible transition shuttle between two intermediate phases contributes to an excellent  $\text{CO}_2$  capture performance for those  $\text{CaO}@x\text{-Al}_2\text{O}_3$  composites.

### Process and economic perspectives of current capture strategy

Because a primary challenge in the commercialization of  $\text{CO}_2$  capture lies in the considerable energy consumption required for sorbent regeneration<sup>44,45</sup>, we quantify the energy requirements for our new strategy. It should be pointed out that the reactions between intermediate phases and  $\text{CO}_2$  are not considered here, given their limited heat effect compared to the reaction between  $\text{CaO}$  and  $\text{CO}_2$  (Supplementary Table 8). From the equilibrium heat required for each  $\text{CO}_2$  cycle (Fig. 5a), our findings indicate that, through an energy balance perspective, the sensible heat within high temperature (700 °C) flue gases can effectively offset the energy needed for sorbent regeneration. This establishes a self-heating system or an exothermic process, resulting in a net energy of  $-6.06$  kJ/g-sorbent (Fig. 5b). Nevertheless, achieving 100% heat transfer efficiency or an equilibrium state in practical applications is challenging. When considering a more realistic heat transfer efficiency of 80%, the practical net energy significantly rises to a substantial positive value of  $47.72$  kJ/g-sorbent, indicating a substantial energy input required for this system. Therefore,

improving the heat transfer efficiency accounts for a vital step for current  $\text{CaO}$ -based  $\text{CO}_2$  capture from high temperature flue gases. Another key process parameter is the carbonation temperature regarding different flue gases since a lower carbonation temperature could affect both the carbonation kinetics and energy/material costs, which could necessitate further explorations.

Building upon the preceding process energy and material analyzes, an economic assessment is conducted per tonne of  $\text{CO}_2$  captured, assuming an 80% heat transfer efficiency. It should be pointed that attrition/fragmentation, as an additional variable affecting energy and material costs, warrants further study for the prospective utilization of the newly developed composites in potential reactors, such as a fluidized bed<sup>41–43</sup>. This forward-looking approach considers prevailing factor prices in anticipation of future commercialization (Fig. 5c). Capital/operation and energy costs emerge as the predominant cost factors, overshadowing the relatively minor impact of material costs associated with  $\text{CaO}$  and  $\text{Al}_2\text{O}_3$ . The implementation of a carbon tax would significantly benefit the proposed process with a by-product ( $\text{CaCO}_3$ ) after decarbonation offering a small advantage. With total costs at US\$153.0 and total benefits at US\$103.2, the net cost for capturing one ton of  $\text{CO}_2$  through the current strategy is US\$49.8. Furthermore, to demonstrate the economic feasibility of our composites, we systematically analyze the energy and material costs associated with 20 cycles of pure  $\text{CaO}$  and  $\text{CaO}@ \text{Al}_2\text{O}_3$  sorbents (Fig. 5d). We find  $\text{CaO}@ \text{Al}_2\text{O}_3$  composite has a higher material cost (US\$4.4), a lower energy cost (US\$7.5), and thus overall lower material and energy costs over pure  $\text{CaO}$  (US\$3.1). We further compare the energy and material costs of  $\text{CaO}@ \text{Al}_2\text{O}_3$  composite after 50 cycles and pure  $\text{CaO}$  after 20 cycles (Fig. 5e). As noted, extending the working cycles (from 20 to 50 cycles) results in further reductions in the energy and material costs of the  $\text{CaO}@ \text{Al}_2\text{O}_3$  composite, making them significantly lower than those of pure  $\text{CaO}$  (20 cycles). This further substantiates the advantages of the  $\text{CaO}@ \text{Al}_2\text{O}_3$  composite.

Considering the potential variability in factor prices and their impact on the economic viability of the current strategy, we proceed with an economic sensitivity analysis (Fig. 5f). Heat transfer efficiency, capital/operation costs, energy prices and carbon tax exhibit significant impacts on the net cost/benefit per tonne of  $\text{CO}_2$  captured. A 50% reduction in capital/operation costs enhances the net economics by US\$50. A 10% increase in heat transfer efficiency contributes to a US\$28 net value increase, whereas a 10% decrease leads to a US\$34 decrease. A 50% surge in energy prices decreases the net value by US\$23 and conversely, a 50% decrease increases the net value by US\$23. The carbon tax constitutes the primary benefit, and a 50% increase of carbon tax improve the net value by US\$50. In contrast, the impact of material and by-product prices is limited, with a 50% increase in material price causing a net value decrease by US\$3. It is worth noting that when heat transfer efficiency increases by 10%, we can have a very low net cost of carbon capture (US\$22 per tonne of  $\text{CO}_2$  captured). Furthermore, two extreme cases with a 50% decrease in capital/operation costs or a 50% increase in carbon tax allow for the development of a near-zero-cost process, underscoring the promising outlook and clear objectives of this new strategy.

In summary, we have designed a novel method to yield highly effective  $\text{CaO}@ \text{Al}_2\text{O}_3$  composites for  $\text{CO}_2$  capture, which involves initially controlling the alumina phases ( $x\text{-Al}_2\text{O}_3$ ) and subsequently sintering  $\text{CaO}$  with  $x\text{-Al}_2\text{O}_3$ . Based on this new method, we successfully induce the formation of  $\text{Ca}_3\text{Al}_2\text{O}_6$  and  $\text{Ca}_5\text{Al}_6\text{O}_{14}$  intermediate phases in  $\text{CaO}@ \delta\text{-Al}_2\text{O}_3$  composite while ensuring a high proportion of active  $\text{CaO}$ . A reversible transition reaction between  $\text{Ca}_3\text{Al}_2\text{O}_6$  and  $\text{Ca}_5\text{Al}_6\text{O}_{14}$  continuously works upon long-term cycling, which contributes to a considerably improved structure stability of  $\text{CaO}@ \delta\text{-Al}_2\text{O}_3$  composite. The target incorporation of stable intermediate phases and intermediate reactions, to prevent deactivation of materials, provides new ideas to improve structure-stability for future material design and

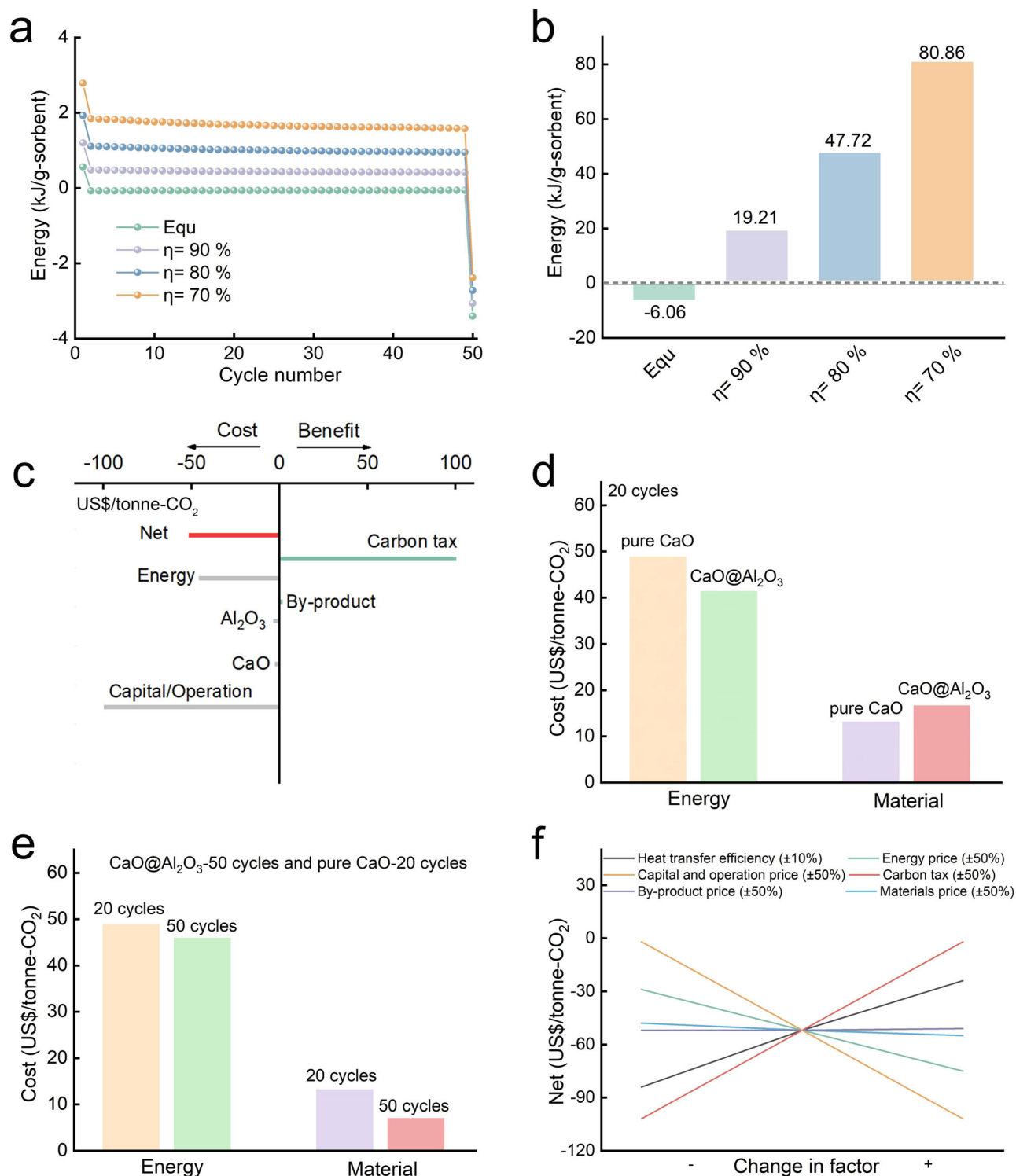


**Fig. 5 | Process and economic analyzes for current CaO-based carbon capture.**

**a** Energy required per gram of CaO-based sorbent for each cycle. **b** Total energy required per gram of sorbent for 50 cycles. **c** Economic assessment per tonne of CO<sub>2</sub> captured at a heat transfer efficiency of 80% for future CaO-based carbon capture. **d, e** Comparison of energy and materials costs of (d) pure CaO and CaO@Al<sub>2</sub>O<sub>3</sub> sorbents working for 20 cycles and (e) CaO@Al<sub>2</sub>O<sub>3</sub> sorbent working for 50 cycles and pure CaO for 20 cycles. **f** Economic sensitivity analysis identifying the roles of key cost and benefit factors. Economic

and economic sensitivity analyzes per tonne of CO<sub>2</sub> captured (**c–f**) are based on the process energy and material analyzes per gram of CaO-based sorbent (**a, b**) as well as those practical factors' prices. Equ represents the equilibrium net energy required for a carbonation-decarbonation cycle singly based on energy balance with a heat transfer efficiency of 100%, and η represents practical heat transfer efficiency. We use the same value for different steps in a whole process to simplify the estimations and the cases of Equ, 90%, 80% and 70% are analyzed in this study.



development. Process and economic assessments further prove that heat transfer efficiency as process factor, capital/operation and energy as costs and carbon tax as benefits dominantly affect the future commercial perspective of current new strategy.

## Methods

### Material preparation

In this study, analytical reagent  $\gamma$ - $\text{Al}_2\text{O}_3$  ( $\geq 99\%$ , Sigma-Aldrich) and calcium acetate ( $\geq 99\%$ , Sigma-Aldrich) are used for the synthesis of samples. We first fabricate a series of alumina phases,  $\delta$ -,  $\theta$ & $\delta$ - and  $\alpha$ - $\text{Al}_2\text{O}_3$ , by direct calcining  $\gamma$ - $\text{Al}_2\text{O}_3$  at 900, 1000 and 1200 °C for 2 h, respectively. We then prepare  $\text{CaO}@ \gamma$ - $\text{Al}_2\text{O}_3$ ,  $\text{CaO}@ \delta$ - $\text{Al}_2\text{O}_3$ ,  $\text{CaO}@ \theta$ & $\delta$ - $\text{Al}_2\text{O}_3$  and  $\text{CaO}@ \alpha$ - $\text{Al}_2\text{O}_3$  composites based on those novel alumina phases. It should be pointed out that we adopt  $x$ - $\text{Al}_2\text{O}_3$  and  $\text{CaO}@x$ - $\text{Al}_2\text{O}_3$  to denote the varying alumina phases and the corresponding composites synthesized in this study, respectively. Appropriate masses of calcium acetate and  $x$ - $\text{Al}_2\text{O}_3$ , with a  $\text{CaO}/\text{Al}_2\text{O}_3$  mass ratio of 8:2, are weighed and mixed to ball milling for 6 h at a rotational speed of 800  $\text{r min}^{-1}$ . Following this, the mixtures are heated with a ramp rate of 5 °C  $\text{min}^{-1}$  and sintered at 900 °C for 2 h to yield the designed  $\text{CaO}@x$ - $\text{Al}_2\text{O}_3$  composites. In addition, for comparative analyzes, pure CaO is also utilized for further  $\text{CO}_2$  capture tests, which is prepared by calcining calcium acetate using the identical sintering process as that of the  $\text{CaO}@x$ - $\text{Al}_2\text{O}_3$  composites.

### Material characterization

The phases and crystallinity of  $x$ - $\text{Al}_2\text{O}_3$  and  $\text{CaO}@x$ - $\text{Al}_2\text{O}_3$  composites are first characterized using an X-ray diffraction (XRD, D/max 2500, Rigaku) technique with a  $\text{Cu K}\alpha$  radiation ( $\lambda = 1.5418 \text{ \AA}$ ). A scanning voltage of 40 kV and a current of 40 mA are used. Both the  $x$ - $\text{Al}_2\text{O}_3$  and the composites are scanned in the  $2\theta$  range of 10–80° with a step size of 0.013° and a scan rate of 4°  $\text{min}^{-1}$ . To quantify the intermediate phases in those composites, a  $2\theta$  range of 30–35° is further scanned with a step size of 0.013° and a smaller scan rate of 1°  $\text{min}^{-1}$ . Additionally, the phase transitions of  $\text{CaO}@ \delta$ - $\text{Al}_2\text{O}_3$  composite during the 1st and 2nd  $\text{CO}_2$  capture cycles have been tested using in-situ XRD (Empyrean, Panalytical) in a  $2\theta$  range of 30–35° with a scan rate of 2°  $\text{min}^{-1}$ . Raman spectra of those samples are acquired across the Raman shift range of 100–1800  $\text{cm}^{-1}$  using an excitation laser (InVia, Renishaw) with a wavelength of 514 nm. Solid-state  $^{27}\text{Al}$  magic-angle spinning-nuclear magnetic resonance (MAS-NMR) spectra are further recorded to identify the coordination states of Al elements using a single-resonance spectrometer with a 2.5 mm HX probe (Avance NEO, Bruker). We also measure the  $\text{N}_2$  physisorption isotherms of those composites (ASAP2460, Micromeritics) and calculate their pore size distributions. X-ray photoelectron spectroscopy (XPS, ESCALab250Xi, Thermo Fisher Scientific) is further employed to investigate the surficial chemical states of the elements in those samples (Al 2p, Ca 2p, and O 1s).

Moreover, to clarify the morphological evolutions of those  $\text{CaO}@x$ - $\text{Al}_2\text{O}_3$  composites, a comprehensive range of characterization techniques are employed. A high-resolution field-emission scanning electron microscopy (FE-SEM, Sigma 300, Zeiss) is utilized to visualize the samples. Prior to imaging, the samples are sputter-coated (Quorum SC7620, Oxford) with Au to improve their conductivity. A secondary electron detector (SE2, JEOL) equipped with an energy-dispersive X-ray (EDX, Smartedx) is used to map the Ca, Al and O elements. When capturing the morphology and EDX mappings of the samples, the operating voltage is set to 3 and 15 kV, respectively. Transmission electron microscopy (TEM, JEM-F200, JEOL) equipped with a large collection-angle EDX (JED-2300T, JEOL) detector is utilized to analyze the microstructures of the samples as well as to identify the local phases at a high resolution (HTEM). Before the TEM tests, the sample powders are dispersed into an ethanol solution for ultrasound, and then a few drops of the dispersed liquid are taken and dripped on the Cu grids, which can be used for testing after thorough drying. The

operating voltage is set to 200 kV in TEM, HTEM and EDX mappings modes.

### Performance characterization

Next, the  $\text{CO}_2$  capture performance of those  $\text{CaO}@x$ - $\text{Al}_2\text{O}_3$  composites synthesized is clarified based on the weight changes from thermogravimetric analysis (Themys, Sataram). A ramp rate of 50 °C  $\text{min}^{-1}$  is used for all heating and cooling processes. The samples ( $\sim 10$  mg) are loaded in a 90  $\mu\text{l}$  platinum crucible and first heated to 900 °C under a  $\text{N}_2$  flow (100  $\text{ml min}^{-1}$ ). After calcination for 10 min, the samples are cooled down to 700 °C and the cyclic tests start with a carbonation reaction under a  $\text{CO}_2$  flow (120  $\text{ml min}^{-1}$ ) for 30 min. The carbonated samples then undergo a decarbonation reaction by raising the temperature to 900 °C in an  $\text{N}_2$  atmosphere (100  $\text{ml min}^{-1}$ ). The samples are then held at this temperature for 10 min. The carbonation and decarbonation stages are repetitively carried out for designed cycles. We further test the  $\text{CO}_2$  capture performance of  $\text{CaO}@ \delta$ - $\text{Al}_2\text{O}_3$  composite over 10 cycles, involving a carbonation in a mixing gas (15 and 1.5 vol. %  $\text{CO}_2$  in  $\text{N}_2$  for 30 min) and a decarbonation in pure  $\text{CO}_2$  for 10 min, to represent more practical scenarios. Simultaneously, the weight changes of the composites are continuously monitored and recorded during the entire operations. To eliminate any potential influence of the crucible quality, blank experiments are conducted using a platinum crucible to calibrate the results, following the same testing procedure as that of the samples. This ensures that any observed weight changes are solely attributed to the reactions of the samples but not affected by the crucible used.

### Thermodynamic calculation

In this study, we conduct a systemic thermodynamic analysis along with the experiments to clarify our concept. The thermodynamic calculation process consists of three main parts. First, a binary phase diagram of CaO and  $\text{Al}_2\text{O}_3$  is calculated by a FactSage 8.1 software (Thermfact/CRCT and GTT-Technologies) using a “Phase Diagram” module<sup>46</sup>. Two databases are selected, namely FactPS and FToxid. This phase diagram serves as a crucial theoretical tool that guides the design of our experimental procedures. Second, we employ a “Reaction” module within FactSage to calculate the Gibbs free energy change ( $\Delta G$ ) for some target reactions such as those for  $\text{Ca}_3\text{Al}_2\text{O}_6$ . Third, those calculations also help us to further determine the  $\Delta G$  values for other target equations not in the databases such as those for  $\text{Ca}_5\text{Al}_6\text{O}_{14}$ . Those calculation results allow us to identify the thermodynamic feasibility of the key reactions and phase transitions in our system more accurately (as detailed in Supplementary Note 1) along with those experimental results.

### Process and economic assessments

Utilizing the thermodynamic data of the base reactants and the performance data of the  $\text{CaO}@ \text{Al}_2\text{O}_3$  composite (Supplementary Tables 9,10), we perform calculations to determine the energy per cycle of the composite for 50 cycles, as well as the total energy required for the entire process. In this part, we consider that the heat transfer efficiency ( $\eta$ ) is at equilibrium, that is, 100%. Additionally, we conduct the same calculations while varying  $\eta$  from equilibrium to 90%, 80%, and 70 %, respectively. An  $\text{CO}_2$  capture process comprises 7 essential steps, outlined in Supplementary Table 10. The initial or 1st step involves heating the sample from 25 to 700 °C. The 2nd step maintains a carbonation temperature for  $\text{CO}_2$  capture. Following the carbonation process, the sample is heated to 900 °C, requiring additional heat absorption. In the 4th step, the sample is heated at 900 °C for releasing  $\text{CO}_2$ . The 5th step involves the temperature decreasing to 700 °C, marking the the beginning of a new cycle. The 6th step includes cooling the sample from 900 to 25 °C, aiming to recover heat from decarbonated  $\text{CO}_2$  as it cools to room temperature. The 7th step, for the final carbonation cycle, involves decreasing the temperature

from 700 to 25 °C without decarbonation. The 1st cycle encompasses steps 1-6, while the final cycle comprises steps 2 and 7. Steps 2-6 work in all other cycles. The detailed calculation process is presented in Supplementary Note 2.

Based on the process analysis results, as well as the prices of each input factor and product, the costs and benefits of different factors can be estimated. First, because the prices of input factors and products, obtained from the pilot-scale trials and market prices<sup>47-52</sup>, are quite different in various regions, they are harmonized considering global income and labor levels<sup>53</sup>. Second, based on the energy balance, the corresponding energy is transformed into electricity with a constant price<sup>54</sup>. The prices of the individual input factors and products after harmonization and the related conversion parameters are summarized in Supplementary Table 11. Third, we calculate the costs and benefits of the whole process based on the process analysis results, and further analyze its economic sensitivity according to the changes in costs and benefits caused by variations in multiple factors.

## Data availability

The main data that support the findings of this study have been included in the main text and Supplementary Information. All other information can be obtained from the corresponding author upon request. Source data are provided with this paper.

## References

1. UNFCCC, Process and meetings, The Paris Agreement. <https://unfccc.int/> (Accessed 13 July 2023).
2. Camarasa, C. et al. A global comparison of building decarbonization scenarios by 2050 towards 1.5–2 °C targets. *Nat. Commun.* **13**, 3077 (2022).
3. Meinshausen, M. et al. Realization of Paris agreement pledges may limit warming just below 2 °C. *Nature* **604**, 304–309 (2022).
4. Jiang, K. & Ashworth, P. The development of carbon capture utilization and storage (CCUS) research in China: a bibliometric perspective. *Renew. Sust. Energ. Rev.* **138**, 110521 (2021).
5. Shao, B. et al. Synergistic promotions between CO<sub>2</sub> capture and in-situ conversion on Ni-CaO composite catalyst. *Nat. Commun.* **14**, 996 (2023).
6. Gao, W. et al. Industrial carbon dioxide capture and utilization: state of the art and future challenges. *Chem. Soc. Rev.* **49**, 8584–8686 (2020).
7. Dunstan, M. T., Donat, F., Bork, A. H., Grey, C. P. & Muller, C. R. CO<sub>2</sub> capture at medium to high temperature using solid oxide-based sorbents: fundamental aspects, mechanistic insights, and recent advances. *Chem. Rev.* **121**, 12681–12745 (2021).
8. Schellnhuber, H. J., Rahmstorf, S. & Winkelmann, R. Why the right climate target was agreed in Paris. *Nat. Clim. Change* **6**, 649–653 (2016).
9. Donat, F., Florin, N. H., Anthony, E. J. & Fennell, P. S. Influence of high-temperature steam on the reactivity of CaO sorbent for CO<sub>2</sub> capture. *Environ. Sci. Technol.* **46**, 1262–1269 (2012).
10. Oschatz, M. & Antonietti, M. A search for selectivity to enable CO<sub>2</sub> capture with porous adsorbents. *Energ. Environ. Sci.* **11**, 57–70 (2018).
11. Singh, G. et al. Emerging trends in porous materials for CO<sub>2</sub> capture and conversion. *Chem. Soc. Rev.* **49**, 4360–4404 (2020).
12. Xu, Y. et al. Structure and surface insight into a temperature-sensitive CaO-based CO<sub>2</sub> sorbent. *Chem. Eng. J.* **435**, 134960 (2022).
13. Li, C. & Wang, H. Power cycles for waste heat recovery from medium to high temperature flue gas sources from a view of thermodynamic optimization. *Appl. Energ.* **180**, 707–721 (2016).
14. Feng, B.-Q. et al. One-step and sustainable preparations of inert additive-doped CaO-based CO<sub>2</sub> adsorbents by hydrogenation reduction of CaCO<sub>3</sub>. *Chem. Eng. J.* **418**, 129479 (2021).
15. Rajamathi, R., Bhojaraj & Nethravathi, C. Porous CaO-MgO nanostructures for CO<sub>2</sub> capture. *ACS Appl. Nano. Mater.* **4**, 10969–10975 (2021).
16. Ma, X. et al. Preparation of a morph-genetic CaO-based sorbent using paper fibre as a biotemplate for enhanced CO<sub>2</sub> capture. *Chem. Eng. J.* **361**, 235–244 (2019).
17. Naeem, M. A. et al. Optimization of the structural characteristics of CaO and its effective stabilization yield high-capacity CO<sub>2</sub> sorbents. *Nat. Commun.* **9**, 2408 (2018).
18. Ping, H. & Wu, S. CO<sub>2</sub> sorption durability of Zr-modified nano-CaO sorbents with cage-like hollow sphere structure. *ACS Sustain. Chem. Eng.* **4**, 2047–2055 (2016).
19. Huang, C., Xu, M., Huai, X. & Liu, Z. Template-free synthesis of hollow CaO/Ca<sub>2</sub>SiO<sub>4</sub> nanoparticle as a cyclically stable high-capacity CO<sub>2</sub> sorbent. *ACS Sustain. Chem. Eng.* **9**, 2171–2179 (2021).
20. Zhang, X. et al. Investigation on a novel CaO-Y<sub>2</sub>O<sub>3</sub> sorbent for efficient CO<sub>2</sub> mitigation. *Chem. Eng. J.* **243**, 297–304 (2014).
21. Pu, Q. et al. Biomass-derived carbon/MgO-Al<sub>2</sub>O<sub>3</sub> composite with superior dynamic CO<sub>2</sub> uptake for post combustion capture application. *J. CO<sub>2</sub> Util.* **54**, 101756 (2021).
22. Peng, W., Xu, Z., Luo, C. & Zhao, H. Tailor-made core-shell CaO/TiO<sub>2</sub>-Al<sub>2</sub>O<sub>3</sub> architecture as a high-capacity and long-life CO<sub>2</sub> sorbent. *Environ. Sci. Technol.* **49**, 8237–8245 (2015).
23. Shen, C., Shen, L., Yan, J., Wang, P. & Yin, X. Inhibitory effect of Na and Al on the sintering phenomenon of calcium-based sorbents during calcium looping. *Energ. Fuel.* **35**, 13871–13876 (2021).
24. Han, R., Gao, J., Wei, S., Su, Y. & Qin, Y. Development of highly effective CaO@Al<sub>2</sub>O<sub>3</sub> with hierarchical architecture CO<sub>2</sub> sorbents via a scalable limited-space chemical vapor deposition technique. *J. Mater. Chem. A* **6**, 3462–3470 (2018).
25. Duyar, M. S., Farrauto, R. J., Castaldi, M. J. & Yegulalp, T. M. In situ CO<sub>2</sub> capture using CaO/γ-Al<sub>2</sub>O<sub>3</sub> washcoated monoliths for sorption enhanced water gas shift reaction. *Ind. Eng. Chem. Res.* **53**, 1064–1072 (2014).
26. Xu, P., Zhou, Z., Zhao, C. & Cheng, Z. Catalytic performance of Ni/CaO-Ca<sub>5</sub>Al<sub>6</sub>O<sub>14</sub> bifunctional catalyst extrudate in sorption-enhanced steam methane reforming. *Catal. Today* **259**, 347–353 (2016).
27. Li, Y., Shi, L., Liu, C., He, Z. & Wu, S. Studies on CO<sub>2</sub> uptake by CaO/Ca<sub>3</sub>Al<sub>2</sub>O<sub>6</sub> sorbent in calcium looping cycles. *J. Therm. Anal. Calorim.* **120**, 1519–1528 (2015).
28. Chen, X., Yang, L., Zhou, Z. & Cheng, Z. Core-shell structured CaO-Ca<sub>9</sub>Al<sub>6</sub>O<sub>18</sub>@Ca<sub>5</sub>Al<sub>6</sub>O<sub>14</sub>/Ni bifunctional material for sorption-enhanced steam methane reforming. *Chem. Eng. Sci.* **163**, 114–122 (2017).
29. Li, Z., Cai, N. & Huang, Y. Y. Effect of preparation temperature on cyclic CO<sub>2</sub> capture and multiple carbonation–calcination cycles for a new Ca-based CO<sub>2</sub> sorbent. *Ind. Eng. Chem. Res.* **45**, 1911–1917 (2006).
30. Armutlulu, A. et al. Multishelled CaO microspheres stabilized by atomic layer deposition of Al<sub>2</sub>O<sub>3</sub> for enhanced CO<sub>2</sub> capture performance. *Adv. Mater.* **29**, 1702896 (2017).
31. Kim, S. M. et al. In situ XRD and dynamic nuclear polarization surface enhanced NMR spectroscopy unravel the deactivation mechanism of CaO-based, Ca<sub>3</sub>Al<sub>2</sub>O<sub>6</sub>-stabilized CO<sub>2</sub> sorbents. *Chem. Mater.* **30**, 1344–1352 (2018).
32. Teixeira, P., Bacariza, C., Mohamed, I. & Pinheiro, C. I. C. Improved performance of modified CaO-Al<sub>2</sub>O<sub>3</sub> based pellets for CO<sub>2</sub> capture under realistic Ca-looping conditions. *J. CO<sub>2</sub> Util.* **61**, 102007 (2022).
33. Zhang, M., Peng, Y., Sun, Y., Li, P. & Yu, J. Preparation of CaO-Al<sub>2</sub>O<sub>3</sub> sorbent and CO<sub>2</sub> capture performance at high temperature. *Fuel* **111**, 636–642 (2013).
34. Kovarik, L. et al. Quantification of high-temperature transition Al<sub>2</sub>O<sub>3</sub> and their phase transformations. *Angew. Chem. Int. Ed.* **59**, 21719–21727 (2020).

35. Lee, J., Jeon, H., Oh, D. G., Szanyi, J. & Kwak, J. H. Morphology-dependent phase transformation of  $\gamma$ - $\text{Al}_2\text{O}_3$ . *Appl. Catal. A: Gen.* **500**, 58–68 (2015).
36. Gao, J., Wen, G., Huang, T., Tang, P. & Liu, Q. Effects of the composition on the structure and viscosity of the CaO–SiO<sub>2</sub>-based mold flux. *J. Non-Cryst. Solids* **435**, 33–39 (2016).
37. McMillan, P. & Piriou, B. Raman spectroscopy of calcium aluminate glasses and crystals. *J. Non-Cryst. Solids* **55**, 221–242 (1983).
38. Hayashi, K., Hirano, M., Matsuiishi, S. & Hosono, H. Microporous crystal  $12\text{CaO}\cdot 7\text{Al}_2\text{O}_3$  encaging abundant O-radicals. *J. Am. Chem. Soc.* **124**, 738–739 (2002).
39. Salaudeen, S. A., Acharya, B. & Dutta, A. CaO-based CO<sub>2</sub> sorbents: a review on screening, enhancement, cyclic stability, regeneration and kinetics modelling. *J. CO<sub>2</sub> Util.* **23** (2018).
40. Grasa, G., Martínez, I., Diego, M. E. & Abanades, J. C. Determination of CaO carbonation kinetics under recarbonation conditions. *Energ. Fuel.* **28**, 4033–4042 (2014).
41. Zhang, H. et al. Attrition of CaO-based adsorbent in a laboratory-scale fluidized system. *Powder Technol.* **393**, 368–379 (2021).
42. Coppola, A., Massa, F., Montagnaro, F. & Scala, F. Analysis of the behaviour of limestone sorbents for sorption-enhanced gasification in dual interconnected fluidised bed reactor. *Fuel* **340**, 127594 (2023).
43. Coppola, A., Montagnaro, F., Scala, F. & Salatino, P. Impact fragmentation of limestone-based sorbents for calcium looping: The effect of steam and sulphur dioxide. *Fuel Process Technol.* **208**, 106499 (2020).
44. Li, M., Irtem, E., Iglesias van Montfort, H. P., Abdinejad, M. & Burdyny, T. Energy comparison of sequential and integrated CO<sub>2</sub> capture and electrochemical conversion. *Nat. Commun.* **13**, 5398 (2022).
45. International Energy Agency, Carbon Capture, Utilisation and Storage. <https://www.iea.org/> (Accessed 10 December 2023).
46. Bale, C. W. et al. Reprint of: FactSage thermochemical software and databases, 2010–2016. *Calphad* **55**, 1–19 (2016).
47. Köppl, A. & Schratzenstaller, M. Carbon taxation: a review of the empirical literature. *J. Econ. Surv.* **37**, 1353–1388 (2022).
48. Cohen, S. M., Rochelle, G. T. & Webber, M. E. Optimal operation of flexible post-combustion CO<sub>2</sub> capture in response to volatile electricity prices. *Energ. Procedia* **4**, 2604–2611 (2011).
49. Wang, H., Wu, J.-J., Zhu, X., Liao, Q. & Zhao, L. Energy-environment-economy evaluations of commercial scale systems for blast furnace slag treatment: Dry slag granulation vs. water quenching. *Appl. Energ.* **171**, 314–324 (2016).
50. London Metal Exchange, Metals. <https://www.lme.com/> (Accessed 10 December 2023).
51. Statista, Energy & Environment. <https://www.statista.com/> (Accessed 10 December 2023).
52. Tradewheel, Product. <https://www.tradewheel.com/> (Accessed 10 December 2023).
53. Eurostat, Labour and capital productivity indicators at total economy and industry level. <https://ec.europa.eu/eurostat/en/> (Accessed 10 December 2023).
54. Sun, Y. et al. Decarbonising the iron and steel sector for a 2 °C target using inherent waste streams. *Nat. Commun.* **13**, 297 (2022).

## Acknowledgements

The authors thank the National Natural Science Foundation of China (52274415) and The National Science Fund for Overseas Excellent Young Scholars (21FAA01748) for financial support. This project is also funded by the Australian Research Council (DP230101901, LP220100309 and FT210100589).

## Author contributions

Y.S. conceived the idea, supervised this project and was responsible for writing and editing this paper. X.M. designed and conducted the experiments, and written the original draft of this paper. S.L. performed the Raman and XRD characterizations. Y.H. and S.S. reviewed and revised this paper. X.Z. revised this paper. J.H. gave important suggestions for paper writing and revised this paper. W.W. and L.Z. discussed the results. All the authors discussed the results and commented on the manuscript.

## Competing interests

The authors declare no competing interests.

## Additional information

**Supplementary information** The online version contains supplementary material available at <https://doi.org/10.1038/s41467-024-52016-y>.

**Correspondence** and requests for materials should be addressed to Jingwei Hou, Wanlin Wang or Yongqi Sun.

**Peer review information** *Nature Communications* thanks Ben Anthony, Yingjie Li, Fabio Montagnaro, and the other, anonymous, reviewer(s) for their contribution to the peer review of this work. A peer review file is available.

**Reprints and permissions information** is available at <http://www.nature.com/reprints>

**Publisher's note** Springer Nature remains neutral with regard to jurisdictional claims in published maps and institutional affiliations.

**Open Access** This article is licensed under a Creative Commons Attribution-NonCommercial-NoDerivatives 4.0 International License, which permits any non-commercial use, sharing, distribution and reproduction in any medium or format, as long as you give appropriate credit to the original author(s) and the source, provide a link to the Creative Commons licence, and indicate if you modified the licensed material. You do not have permission under this licence to share adapted material derived from this article or parts of it. The images or other third party material in this article are included in the article's Creative Commons licence, unless indicated otherwise in a credit line to the material. If material is not included in the article's Creative Commons licence and your intended use is not permitted by statutory regulation or exceeds the permitted use, you will need to obtain permission directly from the copyright holder. To view a copy of this licence, visit <http://creativecommons.org/licenses/by-nc-nd/4.0/>.

© The Author(s) 2024